Science of the Total Environment 835 (2022) 155460

Contents lists available at ScienceDirect

Science of the Total Environment

journal homepage: www.elsevier.com/locate/scitotenv

Selective and simultaneous high resolution 2-D imaging of As^{III}, Cr^{III} and Sb^{III} and dissolved oxygen by developing a new DGT technique comprising a hybrid sensor

Mingyi Ren [a,b], Zhilin Zhong [a,b], Shiming Ding [a,c,*], Jingfu Wang [d,**], Zhihui Dai [e], Cai Li [a,b], Jingxin Cao [a,b], Yan Wang [a,c], Zhi Yu [f], Chaosheng Zhang [g]

[a] State Key Laboratory of Lake Science and Environment, Nanjing Institute of Geography and Limnology, Chinese Academy of Sciences, Nanjing 210008, China
[b] University of Chinese Academy of Sciences, Beijing 100049, China
[c] Nanjing EasySensor Environmental Technology Co., Ltd, Nanjing 210018, China
[d] State Key Laboratory of Environmental Geochemistry, Institute of Geochemistry, Chinese Academy of Sciences, Guiyang 550081, China
[e] State Key Laboratory of Ore Deposit Geochemistry, Institute of Geochemistry, Chinese Academy of Sciences, Guiyang 550081, China
[f] School of Hydraulic Engineering, Changsha University of Science& Technology, Changsha 410114, China
[g] School of Geography, Archaeology & Irish Studies, National University of Ireland, Galway, Ireland

HIGHLIGHTS

- A new DGT can measure As^{III}, Cr^{III} and Sb^{III} selectively for speciation analysis.
- Combining DGT and LA-ICP-MS allows simultaneous 2-D imaging of the three analytes.
- Hybrid PO-DGT sensor allows simultaneous 2-D imaging of As^{III}, Cr^{III} and Sb^{III} and O_2
- Consumption of As^{III} and Sb^{III} appeared in rhizosphere sediment of *V. natans*.
- Laboratory calibration and validation of the novel DGT (HR-MPTS DGT) was performed.

GRAPHICAL ABSTRACT

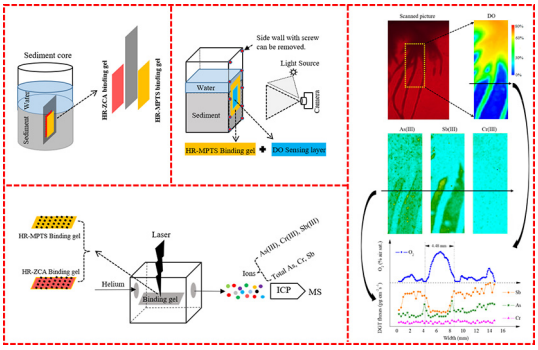

ARTICLE INFO

Editor: Kevin V. Thomas

Keywords:
Arsenic
Chromium
Antimony
Planar optode sensor
Diffusive gradients in thin films

ABSTRACT

A new diffusive gradients in thin films technique (HR-MPTS DGT) with mercapto-functionalized attapulgite in a binding gel was developed for simultaneous two-dimensional (2-D) chemical imaging of As^{III}, Cr^{III} and Sb^{III} selectively at the submillimeter scale, combined with laser ablation inductively coupled plasma mass spectrometry (LA-ICP-MS) analysis. The HR-MPTS DGT exhibited selective accumulation of As^{III}, Sb^{III} and Cr^{III} (> 97%), yet negligible accumulation of As^{V}, Sb^{V} and Cr^{VI} (< 2%). Accumulation of As^{III}, Cr^{III} and Sb^{III} on the binding gel had a linear relationship ($R^2 > 0.99$) with the corresponding standardized laser ablation signals, proving the feasibility of LA-ICP-MS analysis. Analysis for As^{III}, Cr^{III} and Sb^{III} was provided with favorable analytical precision (relative standard deviation <10%). With the purpose of evaluating the dynamics of As^{III}, Cr^{III}, Sb^{III} and O_2 in the rooting zone, a hybrid sensor, which comprises the HR-MPTS gel overlying an O_2 planar optode, was deployed in rhizosphere sediments. Results showed that the consumption of both As^{III} and Sb^{III} due to the oxidation extended ~4.48 mm into the sediments, which was consistent with the extension length of the oxidized sediment layers around the roots created by O_2 leakage.

* Correspondence to: S. Ding, State Key Laboratory of Lake Science and Environment, Nanjing Institute of Geography and Limnology, Chinese Academy of Sciences, Nanjing 210008, China.
** Corresponding author.
E-mail addresses: smding@niglas.ac.cn (S. Ding), wangjingfu@vip.skleg.cn (J. Wang).

http://dx.doi.org/10.1016/j.scitotenv.2022.155460
Received 3 February 2022; Received in revised form 17 April 2022; Accepted 19 April 2022
Available online 23 April 2022

1. Introduction

Arsenic (As), antimony (Sb) and chromium (Cr) are commonly used in industrial processes, but their elevated concentrations accumulated in the environment can cause severe pollution and human health risks owing to their acute toxicity (Chrysochoou et al., 2016; Gorny et al., 2017; Kimbrough et al., 1999; Lee et al., 2015; Wang et al., 2018). (Fan et al., 2019; Ren et al., 2018). Antimonates (Sb^{V}) and antimonites (Sb^{III}) are the commonly found oxidation states in environments (Herath et al., 2017). Compared with Sb^{V} compounds, Sb^{III} compounds are ten times more toxic in spite of their much lower solubility and mobility (Bregoli et al., 2009). Arsenate (As^{V}) and arsenite (As^{III}) are oxidation states of arsenic exist in environments and As^{III} compounds are more toxic than As^{V} compounds (Ferreira et al., 2018). There are two common oxidation states that Cr exists in the natural environment, that is, Cr^{VI} and Cr^{III} (Li et al., 2020). Cr^{VI}, a soluble oxyanion, is highly mobile and toxic, while Cr^{III}, an essential micronutrient for human, is less soluble than Cr^{VI} (Chattopadhyay et al., 2010). The toxicity and bioavailability of As, Cr and Sb in the environment are mainly determined by their chemical speciation. As a result, it is crucial to measure their speciation for better understanding of their environmental impacts.

The element speciation may be altered using traditional sampling methods when samples are collected, transported and treated. Therefore, an in situ passive sampling method, diffusive gradients in thin films technique (DGT) (Davison and Zhang, 1994), has been used widely to measure various elements and chemical compounds in the natural environment (Li et al., 2018). In this method, various elements and chemical compounds in the natural environment accumulated in a defined area of the binding layer is eluted, with resolution at the millimeter scale. Considering the heterogeneous bio-geochemistry of the sediments, two-dimensional (2-D) imaging is necessary for better understanding the biogeochemical processes. The 2-D imaging of various of elements had been realized using DGT coupled to laser ablation inductively coupled plasma mass spectrometry (LA-ICP-MS) analysis at the sub-millimeter scale (Shi et al., 2018; Warnken et al., 2004). Moreover, simultaneous measurement, especially 2-D imaging of multiple elements, ensures both the congruent deployment conditions and spatial resolution and the easier interpretation of data. To date, simultaneous 2-D imaging of total concentrations of As, Cr and Sb using DGT coupled to LA-ICP-MS analysis has been reported (Ren et al., 2021), while to the best of our knowledge, simultaneous 2-D imaging of As^{III}, Sb^{III} and Cr^{III} has never been studied.

Changes in element speciation depend highly on sediment conditions, including dissolved oxygen (DO) and pH (Ren et al., 2021). In the rhizosphere sediment, root exudates and radial oxygen loss (ROL) may change the microbial processes and sediment redox conditions locally, thus influencing the speciation transformation of As, Cr and Sb and their uptake by plants (Martin et al., 2018; Sun et al., 2018; Wagner et al., 2020a, 2020b). Recently, various solutes (such as Mn^{2+}, Fe^{2+}, pH, pCO_2 and NH_4^+) in sediments or soils have been measured at high resolution using a planar optode (Davison, 2016; Glud et al., 1996; Koren and Zieger, 2021; Santner et al., 2015; Smolders et al., 2020; Wagner et al., 2020a, 2020b; Zhu et al., 2015; Zhu, 2019). The combination of DGT and planar optode (PO) sensors has been proved as a promising approach for simultaneous measurement of numerous analytes, such as O_2, pH, the dynamics of labile phosphorus/sulfur/trace metals in sediments, soil and rhizospheres (Li et al., 2019). It is desirable to enable 2-D imaging of element species in combination with the uses of DGT and PO.

In this study, a novel high-resolution DGT (HR-MPTS DGT) technique with (3-mercaptopropyl)-trimethoxysilane (MPTS) containing in the binding gel was developed, and combined with LA-ICP-MS analysis for simultaneous 2-D chemical imaging of As^{III}, Sb^{III} and Cr^{III} at the sub-millimeter scale. The HR-MPTS DGT was further applied in *Vallisneria natans* rhizosphere sediments, in combination with an O_2 planar optode, to investigate the patterns of As^{III}, Sb^{III} and Cr^{III} mobilization in the rooting zone.

2. Experiments

2.1. Materials and solutions

Solutions were all prepared with deionized water (Milli-Q water with 18.2 MΩ cm resistivity, Millipore). All containers were first immersed in 25% (*v*/v) HNO_3 for about 48 h and then rinsed three times using deionized water. Unless otherwise stated, all other reagents used in the experiments were purchased from the National Standard Substances Center (Beijing, China). The (3-mercaptopropyl)-trimethoxysilane (MPTS) (Sigma-Aldrich, USA) was used for preparation of the adsorb agent. The solid N, N′ - methylene diacrylamide (MBA), Acrylamide and ammonium persulfate (APS) were prepared into organic liquids, combined with liquid N, N, N′, N′ - tetramethylethylenediamine (TEMED) (Amresco, USA) for preparing the binding gel. The diffusive gel was prepared with Agarose (Bio-Rad, USA). The preparation of O_2 planar optode was completed by using Macrolex® fluorescence yellow 10GN (MY) (Kremer Pigments Inc., USA), Platinum (II) 2, 3, 7, 8, 12, 13, 17, 18-octaethyl-21H, 23H-porphyrin (PtOEP) (Frontier Scientific Inc., USA) and polystyrene (PS) (Sigma-Aldrich, USA).

2.2. Preparation of DGT and O_2 planar optode sensors

The diffusive gel (0.80 mm thick) was prepared with agarose (1.5% (m/v)) following Wang et al. (2016). A new adsorb agent was prepared by loading MPTS on attapulgite. In brief, 5.0 g attapulgite powder was weighted and was mixed in deionized water (100 mL) using a homogenizer device (Tissue Master, USA) for 5 min at 13500 r/min. Then, with the addition of 5 mL of MPTS, the mixture was further agitated for 5 min at 13500 r/min. After drying at 80 °C for one night, the adsorb agent was obtained. Then, the HR-MPTS binding gel was prepared as follows: 1.0 g of adsorb agent was ground thoroughly to mix with the polyacrylamide solution (4.0 mL), and 2.5 μL TEMED and 10 μL APS (10%) were then added to produce the gel solution. Next, the gel solution was pipetted between two glass plates which were heated in advance and separated by the plastic spacers to obtain a thickness of 0.40 mm. When polymerized for 30 min, the HR-MPTS binding gel was formed, with all the residual chemicals removed by rinsing the gel with deionized water 2–3 times. Before use, the binding gel was kept in a 0.01 $mol{\cdot}L^{-1}$ NaCl solution. The DGTs, for deployment in solutions, consisted in piston-type DGT units (EasySensor Ltd., https://global-easysensor.com), where the HR-MPTS binding gel, the agarose diffusive gel and the filter membrane (here we use the PVDF membrane) were assembled.

The distribution of the adsorb agent in the binding gel was investigated by characterizing the gel with SEM-EDS. Before characterizing, the binding gel was vacuum dried at 50 °C for 4 h, using a vacuum dryer provided by Beijing JUNYI Electrophoresis Co., Ltd. (Beijing, China).

The O_2 planar optode was prepared according to Larsen et al. (2011). Further details are specified in the Supplementary Information (SI). The 0.4 mm thickness of HR-MPTS gel was mounted onto the 2.0 μm thickness of O_2 planar optode. The DGT binding gel was protected by adding a PVDF membrane on top of it, forming a 0.50 mm thickness hybrid sensor for sediment deployments (Fig. 1). A PO2100 device supplied by EasySensor Ltd. was used to perform the Planar optode imaging. In the PO2100 device, two light-emitting diodes arrays (410–420 nm) were used as the excitation light sources. A CCD camera, equipped with a 460 nm long-pass emission filter (Nmot, China) and a macro lens (Fortune Technology, China), was used to capture the fluorescent light images. The resolution of the CCD camera is 4272 × 2848 pixels.

2.3. Characteristics of the HR-MPTS binding gel and the performance of HR-MPTS DGT

2.3.1. Selectivity of the binding gel for As^{III}, Sb^{III} and Cr^{III}

To identify the selectivity of the HR-MPTS binding gel for As^{III}, Sb^{III} and Cr^{III}, the gels were soaked in the 20-mL mixed solutions which contain 100 $\mu g{\cdot}L^{-1}$ of As^{III}, Sb^{III} and Cr^{III} for 48 h. Another series of gels were

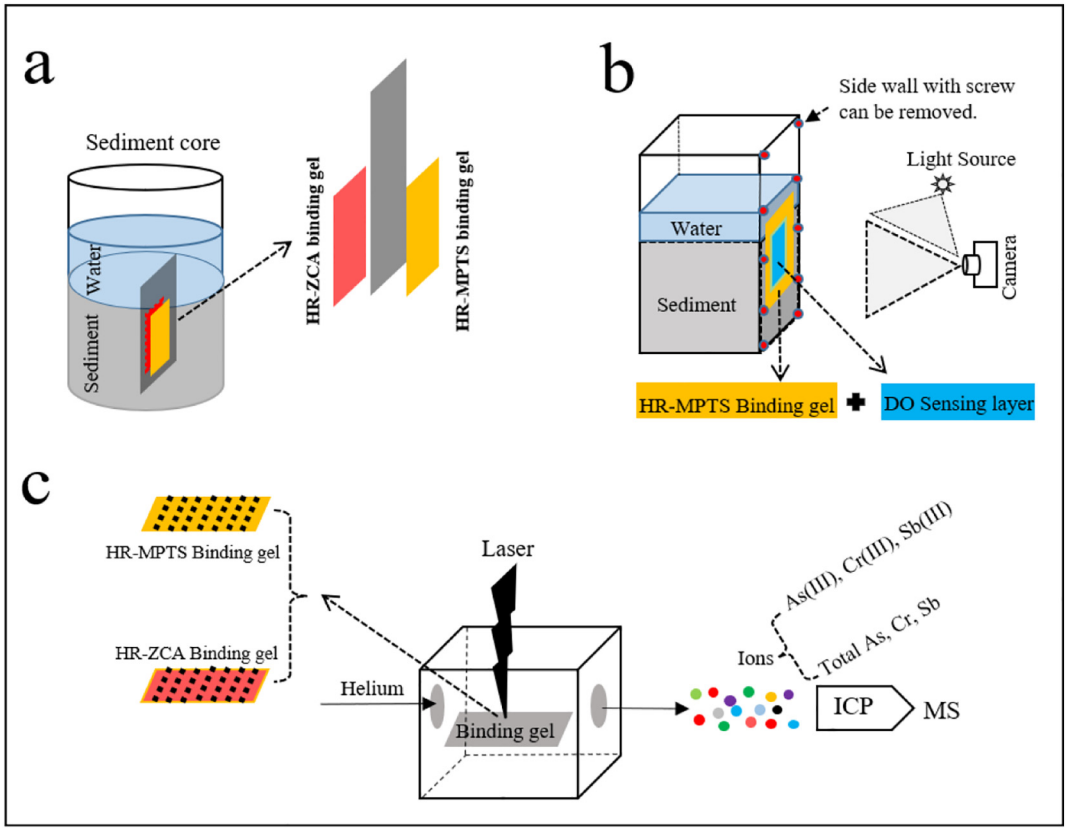

Fig. 1. Diagram of (a) the steel sheet with two different binding gels stuck on each side of it, (b) the combined DGT and PO sensor, and (c) the process of LA-ICP-MS analysis.

soaked in the 20-mL mixed solutions composed of 100 $\mu g \cdot L^{-1}$ of As^{V}, Sb^{V} and Cr^{VI} for 48 h. The concentrations of As, Cr and Sb in the two solutions were determined at 8-h intervals using Agilent 7700× ICP-MS, with the calculation of the uptake efficiencies of As^{III}, As^{V}, Sb^{III}, Sb^{V}, Cr^{III} and Cr^{VI}.

2.3.2. Elution efficiencies of the binding gel for As^{III}, Cr^{III} and Sb^{III}

To ascertain the elution efficiency of the elution solution for As^{III}, Sb^{III} and Cr^{III} adsorbed by the HR-MPTS gel, the gels underwent a 24-h immersion period in the mixed solutions (with a volume of 20 mL) consisting of 100 $\mu g \cdot L^{-1}$ of As^{III}, Sb^{III} and Cr^{III}. The binding gels were then recovered and eluted by immersing them for 24 h in a 1 $mol \cdot L^{-1}$ HNO_3 and 1% KIO_3 solution (20 mL). Afterwards, the elution solutions were analyzed for As, Cr and Sb using Agilent 7700× ICP-MS. The proportion of the amount eluted from the binding gel to the amount adsorbed by the binding gel from the working solutions was used for calculating the elution efficiency of the HR-MPTS gel for As^{III}, Sb^{III} and Cr^{III}.

2.3.3. Performance of HR-MPTS DGT

Further experiments were carried out to study the performance of HR-MPTS binding gel (binding kinetics) and the performance of the HR-MPTS DGT for measurements of As^{III}, Sb^{III} and Cr^{III}, including the effects of pH and ionic strength on the DGT uptake and the capacity of DGT. Further details were provided in the SI2.

2.4. Validation of HR-MPTS DGT in solutions

The HR-MPTS DGT was validated by immersing DGT devices in 10-L mixed solutions containing As^{III}, Cr^{III} and Sb^{III} for 24 h. The DGT devices were retrieved from the solution at temporal intervals of 2, 4, 8, 10, 12, 16, 20 and 24 h. Meanwhile, the concentrations of As^{III}, Cr^{III} and Sb^{III} remaining in the solution and in elution solution as previously described were measured using ICP-MS, with further details specified in the SI. The deployment time was then plotted versus the accumulated masses of As^{III}, Cr^{III} and Sb^{III} in the HR-MPTS gel.

2.5. Quantitative analysis of As^{III}, Cr^{III} and Sb^{III} with LA-ICP-MS analysis

The calibration standards were prepared according to a previous work to certify whether adopting LA-ICP-MS as a quantitative analysis technique was feasible (Ren et al., 2021). Briefly, four DGT devices were immersed in each working solution (2 L volume) containing As^{III}, Cr^{III} and Sb^{III} with varying concentrations of each element (0, 10, 20, 40, 80 and 100 $\mu g \cdot L^{-1}$). The purpose of using different concentrations is to prepare gels with known amounts of elements to be used as standards for LA-ICPMS. After 24 h deployment, the binding gels of three DGTs were eluted before the measurement of As^{III}, Sb^{III} and Cr^{III} by ICP-MS. The remaining DGT binding gel was vacuum dried at 50 °C for 4 h, using a vacuum dryer, before the LA-ICP-MS analysis. The LA-ICP-MS analysis was launched on the basis of the randomly selected laser points (~500) in the center of the dried gels. The precision was tested by calculating the mean and relative standard deviation (RSD) values of these laser ablation signals (standardized).

Laser ablation was conducted with the Resolution LR/S155 laser ablation system equipped with Coherent Compex-Pro 193 nm ArF excimer laser. In addition, Agilent 7700× ICP-MS was used to obtain the signal intensities of target solute. Lehto et al. suggested that ^{13}C can be used as an internal normalization standard (Lehto, 2012). The summary of the operating conditions appropriate for LA and ICP-MS analysis through test experiments is shown in Table S1.

2.6. Application of the DGT in sediment

To test the feasibility of combining DGT and LA-ICP-MS analysis under realistic conditions, the HR-MPTS binding gel was deployed in sediments. The DGT labile As^{III}, Cr^{III} and Sb^{III} fluxes obtained with HR-MPTS gel were compared with the total As, Cr and Sb [As(T), Cr(T) and Sb(T)] fluxes,

which were obtained with a previously reported HR-ZCA binding gel (Ren et al., 2021). Sediment cores and overlying water were collected from Meiliang Bay (31°26′18" N, 120°11′12" E) in Lake Taihu (Jiangsu Province, China). To ensure that the data obtained from the two binding gels were from the same sediment profile, a thin steel sheet (~2 mm thickness) with an HR-ZCA binding gel fixed on one side and an HR-MPTS binding gel fixed on the other side was inserted into the sediment (Fig. 1). The steel sheet was deployed for 24 h, and then both binding gels were retrieved and analyzed by LA-ICP-MS.

2.7. Application of the DGT-PO hybrid sensor in rhizosphere sediment

2.7.1. Calibration of the planar optode

The planar optode of the hybrid sensor was calibrated following Christel et al. (2016). The hybrid sensor (2 × 2 cm) was secured on the interior wall of a transparent cuboid box using adhesive tape. Meanwhile, the box was filled with deionized water to immerse the hybrid sensor. DO levels in the deionized water was adjusted with an air pump (Eheim, Germany). At different DO levels, planar optode imaging was carried out. The equilibrium time refers to the time required by the planar optode to stabilize its fluorescence intensity. The equilibration time was decided to be 10 min in view of the thickness of the hybrid sensor, with the methodology specified in details in the SI3.

2.7.2. Rhizosphere sediment measurements

Vallisneria. natans was collected from Taihu Lake and cultured in the laboratory for propagation. Sediment cores were collected from Taihu Lake. The Perspex boxes with a size of 10 × 10 × 20 cm were transparent and one of their side walls could be removed. Sediment cores were divided at an interval of 2 cm which were then put in the boxes based on their initial depths. Afterwards, the side wall of the box was removed following by sticking the *V. natans* into sediment. The inclined box of 45° promoted the root to grow along the interior wall. After one- month of incubation with air exposure treatment, the side wall was removed and the hybrid sensor was attached onto it (Fig. 1b). These boxes were further incubated for 24 h and the fluorescent images were tracked every 8 h. After the 24-h deployment, the HR-MPTS binding gel was retrieved and dried for LA-ICP-MS analysis.

2.8. Sample analysis and calculation

The dried binding gel was characterized by virtue of scanning electron microscope energy dispersion spectra (SEM-EDS) (ZEISS EVO 18, Germany) to investigate how the adsorb agent is distributed in the HR-MPTS gel. High resolution 2-D images of DGT-labile As^{III}, Cr^{III} and Sb^{III} [or As(T), Cr(T) and Sb(T)] fluxes were obtained using Matlab 2014a software and Surfer 16.0 software.

The accumulated masses of the target solutes on the binding gels (M, ng) (Eq. S3) and the concentration of the target solutes measured by DGT (C_{DGT}, mg/L) (Eq. S4) were respectively calculated as reported by Zhang and Davison (1995). The DGT-labile As^{III}, Cr^{III} and Sb^{III} [or As(T), Cr(T) and Sb(T)] fluxes (F, $\mu g \cdot cm^{-2} \cdot s^{-1}$) were computed in accordance to Li et al. (Eq. S5) (Li et al., 2018).

3. Results and discussion

3.1. SEM-EDS analysis results

When the DGT is combined with LA-ICP-MS analysis, adsorb agents in the binding gel should be sufficiently small (particle size ≤ 10 μm) and evenly distributed in the gel. The distribution of the adsorb agent in the binding gel was investigated by characterizing the vacuum dried gel with SEM-EDS (Fig. 2a). Besides, the peak signal intensities of Mg, S, Si and Al, which are the major elemental components in the adsorb agent, appeared in the gel surface region (Fig. 2c), indicating the uniform distribution of the adsorb agent on the binding gel surface (Fig. 2b).

3.2. Binding gel characteristics and performance of DGT

3.2.1. The uptake efficiencies of the HR-MPTS gel for As, Cr and Sb species

The uptake efficiencies of the HR-MPTS gel for As, Cr and Sb species were calculated and the results are shown in Fig. 3a. After 8 h of adsorption, all the uptake efficiencies of the gel for As^{III}, Sb^{III} and Cr^{III} exceeded 91%, while those for As^{V}, Cr^{VI} and Sb^{V} were ~ 1%. After 48 h of deployment, uptake efficiencies of the gel for As^{III}, Sb^{III} and Cr^{III} were greater than 97%, while those for As^{V}, Cr^{VI} and Sb^{V} were smaller than 2%, confirming that the binding gel can selectively bind As^{III}, Sb^{III} and Cr^{III} with negligible binding of As^{V}, Sb^{V} and Cr^{VI}. Furthermore, the elution efficiencies of the MPTS gel for As^{III}, Cr^{III} and Sb^{III} species were all ~100%.

3.2.2. The adsorption kinetics of the HR-MPTS gel for As^{III}, Sb^{III} and Cr^{III}

The adsorption kinetics of the HR-MPTS gel for As^{III}, Sb^{III} and Cr^{III} were tested with results exhibited in Fig. 3b. The uptake efficiencies of As^{III}, Cr^{III} and Sb^{III} increased with the binding time. Specifically, during the initial exposure period of 120 min, the uptake efficiencies of As^{III}, Cr^{III} and Sb^{III} increased rapidly, reaching 84%, 73% and 81%, respectively. After 120 min, the uptake efficiencies began to increase slowly and level off at 180 min. After 180 min, all the uptake efficiencies for As^{III}, Cr^{III} and Sb^{III} reached ~90%, among which the binding rate of Cr^{III} (88%) was higher than that of Sb^{III} (87%) or As^{III} (86%). The average binding rates for As^{III}, Cr^{III} and Sb^{III} in the first 10 min were 7.9, 3.2 and 7.0 $ng \cdot cm^{-2} \cdot min^{-1}$, respectively. A diffusion layer (diffusive gel plus filter membrane) with a 0.09 cm thickness was adopted to calculate the DGT-measured fluxes in the mixed solution containing 50 $\mu g \cdot L^{-1}$ of As^{III}, Sb^{III} and Cr^{III}. The respective DGT-measured flux for As^{III}, Cr^{III} and Sb^{III} was 0.26, 0.43 and 0.073 $ng \cdot cm^{-2} \cdot min^{-1}$. The ratios between the binding rate and the DGT-measured flux for As^{III}, Cr^{III} and Sb^{III} were respectively 30, 7 and 96, demonstrating that it was quick enough for the absorption kinetics of the binding gel in terms of As^{III}, Cr^{III} and Sb^{III} to satisfy the DGT uptake.

3.2.3. The diffusion coefficient for As^{III}, Sb^{III} and Cr^{III}

The deployment time was plotted versus the accumulated masses on the binding gel and the Eq. (S1) was used to calculate diffusion coefficient with the slope of the generated curves. The effective diffusion coefficients for As^{III}, Sb^{III} and Cr^{III} were respectively calculated as 8.2, 8.9 and 2.2 ($\times 10^{-6}$ $cm^2 \cdot s^{-1}$, 25 °C). The estimated diffusion coefficients of Sb^{III} in other studies were 9.42 and 8.23 ($\times 10^{-6}$ $cm^2 \cdot s^{-1}$, 25 °C), respectively (Bennett et al., 2016), which were consistent with data in this study. In addition, a diffusion coefficient of 9.04 × 10^{-6} $cm^2 \cdot s^{-1}$ (25 °C) has been reported for As^{III}, which agrees relatively well with the diffusion coefficient for As^{III} in this study (Bennett et al., 2016). The estimated diffusion coefficients of Cr^{III} in other studies were 5.05 ($\times 10^{-6}$ $cm^2 \cdot s^{-1}$, 25 °C) (https://www.dgtresearch.com), which was higher than the value in this study.

3.2.4. The influence of pH and ionic strength on DGT measurement of As^{III}, Sb^{III} and Cr^{III}

Typically, C_{DGT} is used to represent the DGT-measured concentration and C_{Sol} is used to represent the substrate concentration in solution. The feasibility of DGT measurements can be proved with the C_{DGT}/C_{Sol} values ranging from 0.90 to 1.1 (Zhang and Davison, 1995). Given the range of the C_{DGT}/C_{Sol} values from 0.9 to 1.1 and that of the pH values from 3.2 to 8.2 for the measurements of As^{III}, Cr^{III} and Sb^{III}, it was clear that within a pH range of 3.2–8.2, DGT uptake was not affected by the change of pH values (Fig. 3c). The influence of the pH range on other DGT measurements of As^{III} and Sb^{III} has been reported previously, showing relatively good agreement with our DGT results (Bennett et al., 2010; Bennett et al., 2011; Bennett et al., 2016; Fang et al., 2020). In a previous study, the range of pH in which DGT measurement of Cr^{III} is not influenced was 2–5, which was due to the fact that Cr^{III} was stable in the solution with a pH below 5, thus the experiment was performed in the pH ranging from 2 to 5 (Ernstberger et al., 2002). However, when Cr^{III} in solution is at labile equilibrium, the binding gel can bind Cr^{III} directly and DGT can also

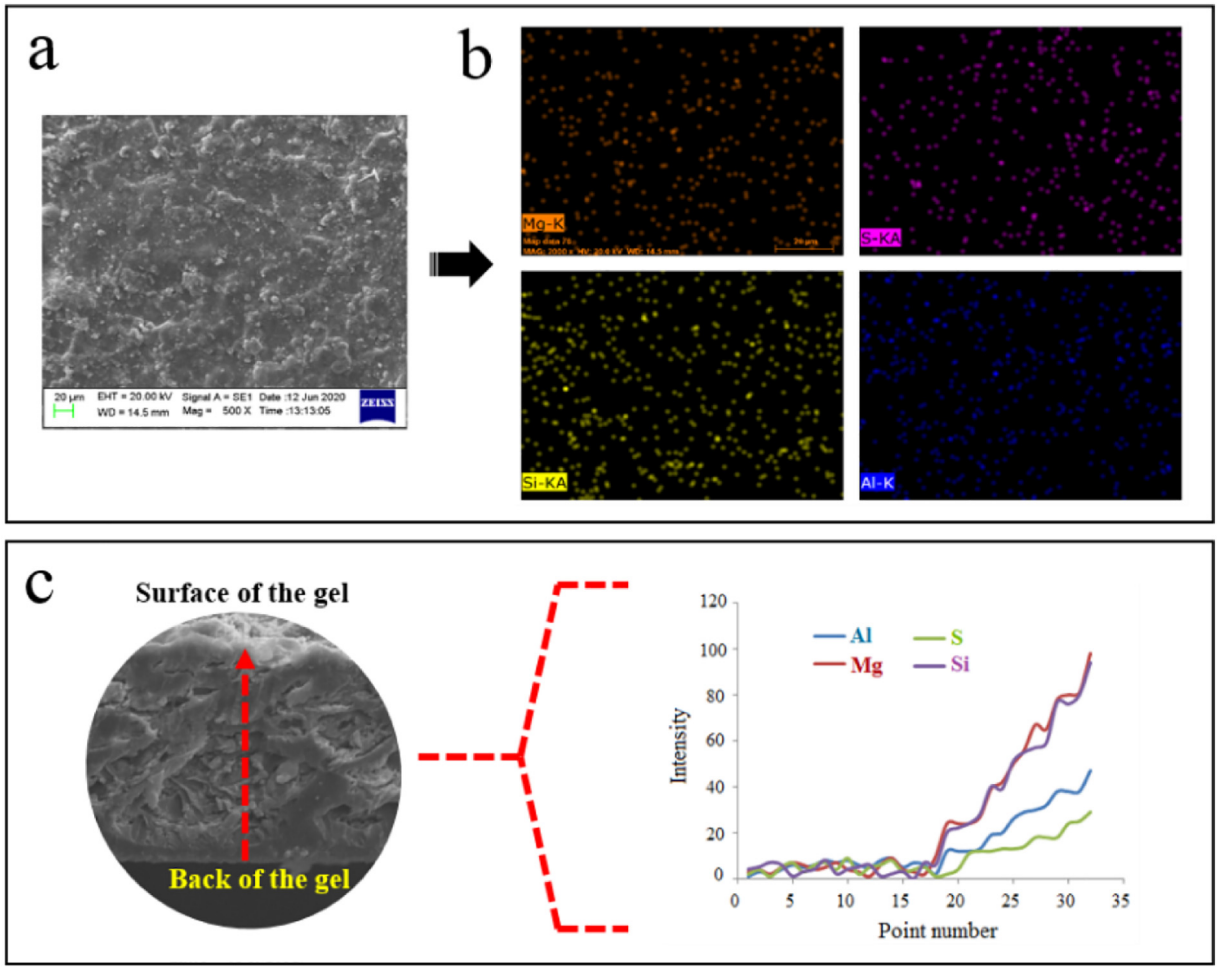

Fig. 2. SEM-EDS images about the HR-MPTS binding gel: (a) image of the gel surface; (b) element distribution of the gel; (c) cross-section image of the gel, in which the red arrow indicates the direction from the back to the surface of the gel.

measure Cr^{III} (Ernstberger et al., 2002), and the results in this study showed that HR-MPTS DGT uptake of Cr^{III} was independent of pH 3.2–8.2.

In addition, there was no effect on the DGT uptake of As^{III}, Sb^{III} and Cr^{III} when the ionic strength was below 1000, 1000 and 200 mmol·L^{-1} NaCl (Fig. 3d). The upper limit of the NaCl concentration for HR-MPTS measurement of As^{III} (1000 mmol·L^{-1}) was higher than that for mercapto-silica and Metsorb DGT (750 mmol·L^{-1}) (Bennett et al., 2010; Bennett et al., 2011). The maximum NaCl concentration of HR-MPTS measurement of Sb^{III} (1000 mmol·L^{-1}) was higher than that of MSBA DGT (200 mmol·L^{-1}) (Fang et al., 2020), but it was in line with the recorded limit for mercapto-silica and Metsorb DGT (1000 mmol·L^{-1}) (Bennett et al., 2016). The upper limit of the NaCl concentration for HR-MPTS measurement of Cr^{III} (200 mmol·L^{-1}) was higher than the upper limit of the $NaNO_3$ concentration for Chelex-100 DGT measurement of Cr^{III} (100 mmol·L^{-1}) (Devillers et al., 2016).

3.2.5. DGT capacities for As^{III}, Sb^{III} and Cr^{III}

To calculate the DGT capacities for As^{III}, Cr^{III} and Sb^{III}, the accumulated masses of As^{III}, Cr^{III} and Sb^{III} on the DGT devices over time was examined (Fig. 3e). For As^{III}, Cr^{III} and Sb^{III} masses, there was a linear increase to 20, 16 and 16 h, when the accumulation tended to stabilize. Considering the 3.14 cm^2 exposure surface, the DGT capacities for As^{III}, Sb^{III} and Cr^{III} measurement were calculated to be 72, 79 and 44 µg·device^{-1}, respectively. The HR-MPTS DGT capacity for Sb^{III} is higher than that reported for MSBA DGT (65 µg·gel^{-1}) (Fang et al., 2020), but lower than that reported for mercapto-silica DGT and Metsorb DGT (100 µg·gel^{-1}) (Bennett et al., 2016). In addition, the HR-MPTS DGT capacity for As^{III} was much higher than that reported with Metsorb DGT (8.5 µg·gel^{-1}) and almost the same as that for mercapto-silica DGT (77.5 µg·gel^{-1}) (Bennett et al., 2016).

3.3. Validation of HR-MPTS DGT in solutions

The relationship between the accumulated masses of As^{III}, Cr^{III} and Sb^{III} in the HR-MPTS gel and the deployment time was examined to validate the HR-MPTS DGT (Fig. 4). The estimated masses of As^{III}, Cr^{III} and Sb^{III} were calculated by Eq. (S4), showing that there was a linear increase in As^{III}, Cr^{III} and Sb^{III} masses over time (r^2 for As^{III}, Cr^{III} and Sb^{III} > 0.998). Furthermore, theoretical predicted masses of As^{III}, Cr^{III} and Sb^{III} were calculated by Eq. (S3), which were fairly consistent with the experimental data with the ratio of measured masses to predicted values (measured / predicted) for As^{III}, Cr^{III} and Sb^{III} lying within 1.00 and 1.02. As a result, the use of the HR-MPTS gel was validated feasible for the DGT measurement.

3.4. Analytical performance of LA-ICP-MS

LA-ICP-MS analysis was used to calculate the mass accumulation of As^{III}, Cr^{III} and Sb^{III} in the binding gel in a quantitative manner using the prepared calibration curves. For this, gels were immersed in solutions with different concentrations as standards. The calibration standards were defined according to the plot of standardized laser ablation signals (divide the signals of element by the signals of internal standard ^{13}C) versus mass accumulation on the HR-MPTS gels (per analyzed ablation spot) given in Fig. 5. The accumulated masses on binding gels were in a good linear relationship (r^2 > 0.99) with the corresponding laser ablation signals, which confirmed that it

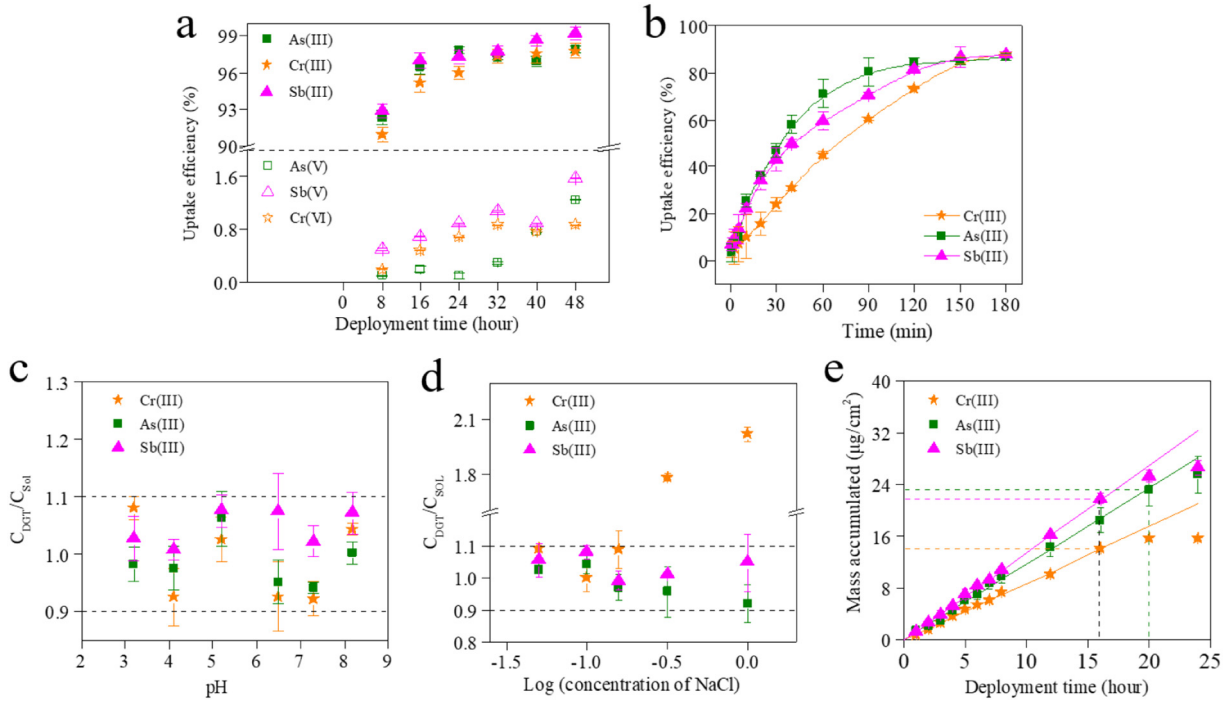

Fig. 3. (a) Uptake efficiencies (%) of As^{III}, Cr^{III}, Sb^{III}, As^{V}, Cr^{VI} and Sb^{V}. (b) Dynamic uptake efficiencies (%) of As^{III}, Cr^{III} and Sb^{III}. Conditions: 50 μg/L of As^{III}, Cr^{III} and Sb^{III}, solution pH 5.5, ionic strength of 1 mM of NaCl, 3 h total deployment time at room temperature. (c) C_{DGT}/C_{Sol} values for As^{III}, Cr^{III} and Sb^{III} under different pH conditions. Conditions: 50 μg/L of As^{III}, Cr^{III} and Sb^{III}, ionic strength of 1 mM of NaCl, 24 h deployment time at room temperature. (d) C_{DGT}/C_{Sol} values for As^{III}, Cr^{III} and Sb^{III} under different concentrations of NaCl. Conditions: 50 μg/L of As^{III}, Cr^{III} and Sb^{III}, solution pH of 5.5, 24 h deployment time at room temperature. C_{DGT}/C_{Sol} values delineated by the two dotted lines are between 0.9 and 1.1. The error bar represents the standard deviation of the three replicates of measurements. (e) DGT capacities for measurement of As^{III}, Cr^{III} and Sb^{III}. Conditions: 1 mg/L As^{III}, Cr^{III} and Sb^{III}, solution pH 5.5, ionic strength featuring 1 mM of NaCl, the 24 h deployment time at room temperature.

is feasible to combine DGT with LA-ICP-MS for quantitative measurements of As^{III}, Cr^{III} and Sb^{III}.

As is shown in Fig. 5, the precision of LA-ICP-MS analysis was assessed by calculating the mean and RSD values of the laser ablation signals (standardized) of the randomly selected laser points on each gel. The analytical precision for As^{III}, Cr^{III} and Sb^{III} was adequate, with a minimum RSD value of 4.3% and the majority of the RSD values being less than 10%.

3.5. Application of the DGT in sediment

The 2-D distributions of DGT-labile As^{III}, Sb^{III} and Cr^{III} fluxes established by HR-MPTS DGT were compared with the 2-D distributions of DGT-labile As(T), Sb(T) and Cr(T) fluxes based on HR-ZCA DGT (Fig. 6a). Fluxes of As^{III}, Sb^{III} and Cr^{III} in sediments corresponded to ~11%, ~17% and ~ 82% of total fluxes, respectively.

The distributions of As^{III} and As(T) fluxes showed similar patterns. In overlying water, fluxes of As(T) (average of 0.8 $pg \cdot cm^{-2} \cdot s^{-1}$) and As^{III} (average of 0.1 $pg \cdot cm^{-2} \cdot s^{-1}$) showed lower values. From the sediment water interface (SWI) to −19 mm depth, fluxes of As(T) increased from 1.1 $pg \cdot cm^{-2} \cdot s^{-1}$ to 7.0 $pg \cdot cm^{-2} \cdot s^{-1}$. And from −4 mm depth to −19 mm depth, fluxes of As^{III} increased from 0.3 $pg \cdot cm^{-2} \cdot s^{-1}$ to 0.8 $pg \cdot cm^{-2} \cdot s^{-1}$. The distributions of Sb^{III} and Sb(T) fluxes also showed similar patterns. In overlying water, fluxes of Sb(T) (average of 0.11 $pg \cdot cm^{-2} \cdot s^{-1}$) and Sb^{III} (average of 0.01 $pg \cdot cm^{-2} \cdot s^{-1}$) showed lower values. From the SWI to −19 mm depth, fluxes of Sb(T) increased from 0.11 $pg \cdot cm^{-2} \cdot s^{-1}$ to 0.23 $pg \cdot cm^{-2} \cdot s^{-1}$. And from −4 mm depth to −19 mm depth, fluxes of Sb^{III} increased from 0.03 $pg \cdot cm^{-2} \cdot s^{-1}$ to 0.04 $pg \cdot cm^{-2} \cdot s^{-1}$. In the overlying water, fluxes of Cr(T) showed higher values (average of 1.5 $pg \cdot cm^{-2} \cdot s^{-1}$). In sediment profiles, fluxes of Cr (T) showed lower values with small fluctuations (average of 1.1 $pg \cdot cm^{-2} \cdot s^{-1}$). In contrast, fluxes of Cr^{III} in the overlying water and sediment profiles had similar values (average of 0.9 $pg \cdot cm^{-2} \cdot s^{-1}$).

Under aerobic conditions, the oxidation of Cr^{III} to Cr^{VI} may lead to the higher fluxes of Cr(T) in the overlying water (Gorny et al., 2017). However,

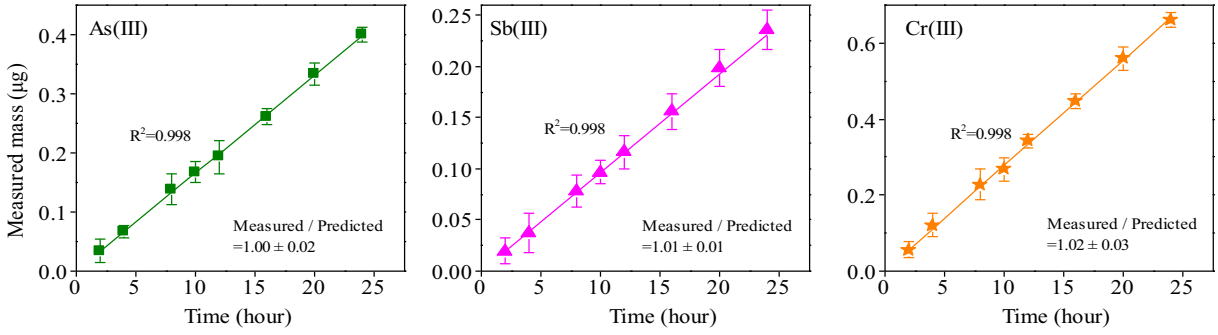

Fig. 4. Relationships between the masses of As^{III}, Cr^{III} and Sb^{III} accumulated in the HR-MPTS DGT devices and the deployment time.

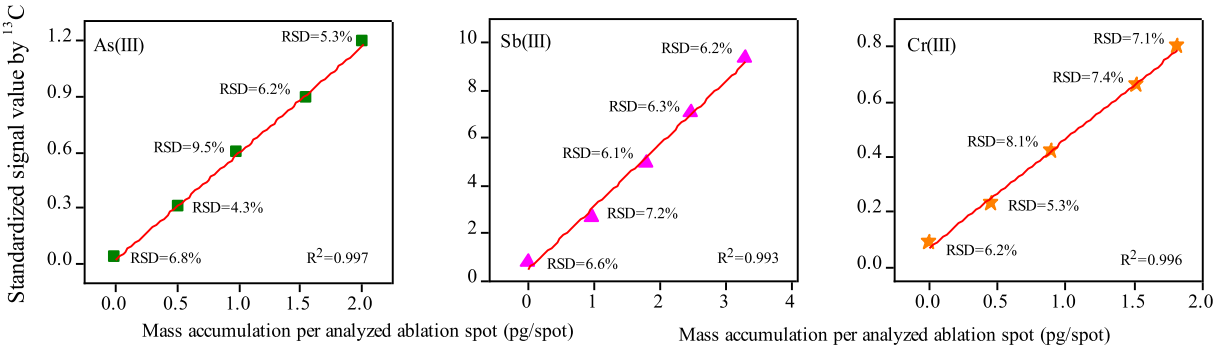

Fig. 5. Relationships between the masses of As^{III}, Cr^{III} and Sb^{III} accumulated in the HR-MPTS binding gels per analyzed ablation spot (pg/spot) and the corresponding standardized laser ablation signals.

Cr^{III} can be combined with natural organic matter, thus increasing the solubility of Cr^{III} in sediments (Li et al., 2020). For As and Sb, As^{V}/Sb^{V} compounds are more soluble than As^{III}/Sb^{III} compounds. In addition, As/Sb are mainly bound to the goethite surface in the natural environment and can be easily oxidized to As^{V}/Sb^{V} under aerobic conditions. As a result, As^{V}/Sb^{V} predominates and As^{III}/Sb^{III} is only found at low concentrations under aerobic conditions (Leuz et al., 2006). Herein, from the SWI to −4 mm depth, the combination of Fe/Mn oxides led to the low fluxes of As and Sb, while the oxidation of As^{III} and Sb^{III} in this area might contribute to the increase in As(T) and Sb(T). As a result, from the SWI to −4 mm

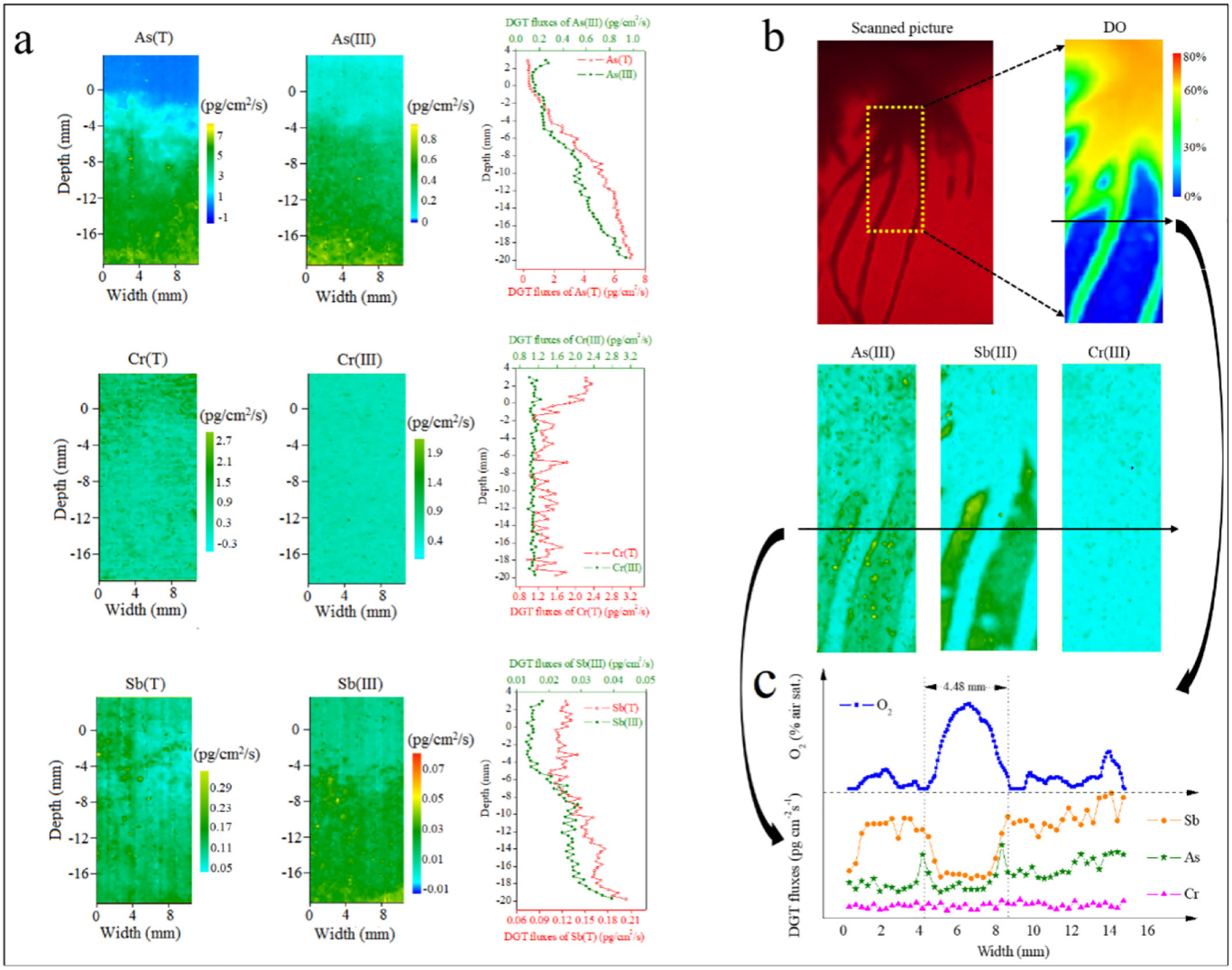

Fig. 6. (a) 2-D and 1-D vertical distributions of DGT-labile fluxes of As(T), Cr(T) and Sb(T) and DGT-labile fluxes of As^{III}, Cr^{III} and Sb^{III} in the sediments of Meiliang Bay, Lake Taihu (1-D vertical distribution of DGT-labile fluxes are at a 0.38 mm resolution). (b) 2-D distributions of DGT-labile fluxes of As^{III}, Cr^{III} and Sb^{III} with LA-ICP-MS analysis and 2-D imaging of O_2 concentrations in rhizosphere sediment. (c) 1-D horizontal distributions of DGT-labile fluxes of As^{III}, Sb^{III} and Cr^{III} at a 0.38 mm resolution and 1-D imaging of O_2 concentrations at a 0.08 mm resolution at a certain sediment depth.

depth, As(T) and Sb(T) fluxes increased, while As^{III} and Sb^{III} showed low values. With the increase in sediment depth, the Fe/Mn oxides were reduced, followed by releasing As and Sb complexed with them, which accounted for the increase in the fluxes of As and Sb (Ren et al., 2021).

Furthermore, from −16 mm to −19 mm depth, As^{III}, As(T), Sb^{III} and Sb(T) fluxes showed almost simultaneous local increases (Fig. 6a). It has been indicated in previous studies that sulfide either undergoes the local reduction of sulfate or diffuses upward from the sulfidic zone to enter the sub-oxic zone. Then at the interface of the sulfidic zone and sub-oxic zone, Fe(III) is reduced by sulfide rapidly (Jørgensen and Nelson, 2004). In this study, the locally increased fluxes of As and Sb (from −16 mm to −19 mm depth) may be ascribed to the oxidation of sulfide by Fe(III), thus releasing As and Sb complexed with Fe-oxides.

3.6. Simultaneous 2-D imaging of As^{III}, Cr^{III}, Sb^{III} and O_2 in rhizosphere sediments

The 2-D distributions of DGT-labile As^{III}, Sb^{III} and Cr^{III} fluxes and 2-D imaging of O_2 concentrations at the end of the 24-h deployment time in rhizosphere sediments are shown in Fig. 6b. The 1-D horizontal distribution of As^{III}, Sb^{III}, Cr^{III} fluxes and O_2 concentrations at a certain sediment depth were mapped (Fig. 6c). Vallisneria. natans is a dominant submerged macrophyte in Lake Taihu (Wang et al., 2020). For *V. natans* with roots in waterlogged sediments, O_2 is transported to the roots to allow their respiration. Part of the transported O_2 may leak out and create an oxidized sediment layer around the roots. Its growth has previously been found to promote the formation of an aerobic microenvironment in the rhizosphere (Marzocchi et al., 2019). In this study, the oxidized sediment layers around the roots extended ~4.48 mm into the sediments. Moreover, the consumption of As^{III} and Sb^{III} concurrently extended ~4.48 mm into the sediments, which was consistent with the extension length of the oxidized sediment layers around the roots created by O_2 leakage. However, the consumption of Cr^{III} was small, with no obvious area of extension into the sediments.

ROL enhanced the oxidation of As^{III} and Sb^{III} bound by Fe/Mn oxides, thus decreasing their fluxes in the rhizosphere (Leuz et al., 2006). It has been indicated that the rhizosphere may be an important barrier against As^{III}/Sb^{III} uptake as bacteria may oxidize the mobile and more toxic As^{III}/Sb^{III} to the less toxic As^{V}/Sb^{V}, thus accounting for the decrease in their fluxes near the roots (Sun et al., 2018). In contrast, ROL may have little influence on the oxidation of Cr^{III}, with no evident change of Cr^{III} in the rhizosphere.

4. Conclusions

The developed HR-MPTS DGT combined with LA-ICP-MS analysis allows the simultaneous and selective measurement of As^{III}, Sb^{III} and Cr^{III}. The uptake efficiencies of the HR-MPTS binding gel for As^{III}, Sb^{III} and Cr^{III} were greater than 97%, while those for As^{V}, Cr^{VI} and Sb^{V} were smaller than 2%, confirming that the binding gel can selectively bind As^{III}, Sb^{III} and Cr^{III} with negligible binding of As^{V}, Sb^{V} and Cr^{VI}. The adsorption kinetics of the gel for As^{III}, Sb^{III} and Cr^{III} was quick enough for the DGT uptake. The effective diffusion coefficients for As^{III}, Sb^{III} and Cr^{III} were 8.2, 8.9 and 2.2 ($\times 10^{-6}$ $cm^2 \cdot s^{-1}$, 25 °C), respectively. The DGT uptake of As^{III}, Sb^{III} and Cr^{III} was not affected within a 3.2–8.2 pH range and below 1000, 1000 and 200 $mmol \cdot L^{-1}$ NaCl, respectively. The DGT capacities for As^{III}, Sb^{III} and Cr^{III} measurement were 72, 79 and 44 $\mu g \cdot device^{-1}$, respectively. The accumulated masses on the HR-MPTS binding gels were in a good linear relationship ($r^2 > 0.99$) with the corresponding laser ablation signals, and the analytical precision for As^{III}, Cr^{III} and Sb^{III} was adequate, with a minimum RSD value of 4.3% and the majority of the RSD values being less than 10%. The measurement of a hybrid sensor comprising the HR-MPTS gel overlying an O_2 planar optode showed that the consumption of both As^{III} and Sb^{III} extended ~4.48 mm into the sediments due to the oxidation around the roots created by O_2 leakage.

CRediT authorship contribution statement

Mingyi Ren: Data curation, Writing – original draft. **Zhilin Zhong:** Investigation. **Shiming Ding:** Conceptualization, Methodology. **Jingfu Wang:** Conceptualization, Methodology. **Zhihui Dai:** Software, Validation. **Cai Li:** Software, Validation. **Jingxin Cao:** Software, Validation. **Yan Wang:** Software, Validation. **Zhi Yu:** Writing – review & editing. **Chaosheng Zhang:** Writing – review & editing.

Declaration of competing interest

The authors declare that they have no known competing financial interests or personal relationships that could have appeared to influence the work reported in this paper.

Acknowledgments

This research work was funded by the National Natural Science Foundation of China (U2102210 and 41877492), the National Key Research and Development Plan (2018YFA0903003), and the Youth Innovation Promotion Association CAS (No.2019389).

Appendix A. Supplementary data

Supplementary data to this article can be found online at https://doi.org/10.1016/j.scitotenv.2022.155460.

References

Bennett, W.W., Teasdale, P.R., Panther, J.G., Welsh, D.T., Jolley, D.F., 2010. New diffusive gradients in a thin film technique for measuring inorganic arsenic and selenium(IV) using a titanium dioxide based adsorbent. Anal. Chem. 82 (17), 7401–7407.

Bennett, W.W., Teasdale, P.R., Panther, J.G., Welsh, D.T., Jolley, D.F., 2011. Speciation of dissolved inorganic arsenic by diffusive gradients in thin films: selective binding of AsIII by 3-mercaptopropyl-functionalized silica gel. Anal. Chem. 83 (21), 8293–8299.

Bennett, W.W., Arsic, M., Welsh, D.T., Teasdale, P.R., 2016. In situ speciation of dissolved inorganic antimony in surface waters and sediment porewaters: development of a thiol-based diffusive gradients in thin films technique for SbIII. Environ. Sci.: Processes Impacts 18 (8), 992–998.

Bregoli, L., Chiarini, F., Gambarelli, A., Sighinolfi, G., Gatti, A.M., Santia, P., Martelli, A.M., Cocco, L., 2009. Toxicity of antimony trioxide nanoparticles on human hematopoietic progenitor cells and comparison to cell lines. Toxicology 262 (2), 121–129.

Chattopadhyay, B., Utpal, S., Mukhopadhyay, S., 2010. Mobility and bioavailability of chromium in the environment: physico-chemical and microbial oxidation of Cr (III) to Cr (VI). J. Appl. Sci. Environ. Manag. 14 (2), 97–101.

Christel, W., Zhu, K., Hoefer, C., Kreuzeder, R., Santner, J., Bruun, S., Magid, J., Jensen, L.S., 2016. Spatiotemporal dynamics of phosphorus release, oxygen consumption and greenhouse gas emissions after localised soil amendment with organic fertilisers. Sci. Total Environ. 554, 119–129.

Chrysochoou, M., Theologou, E., Bompoti, N., Dermatas, D., Panagiotakis, I., 2016. Occurrence, origin and transformation processes of geogenic chromium in soils and sediments. Curr. Pollut. Rep. 2 (4), 224–235.

Davison, W. (Ed.), 2016. Diffusive Gradients in Thin-films for Environmental Measurements. Cambridge University Press.

Davison, W., Zhang, H., 1994. In situ speciation measurements of trace components in natural waters using thin-film gels. Nature 367 (6463), 546–548.

Devillers, D., Buzier, R., Simon, S., Charriau, A., Guibaud, G., 2016. Simultaneous measurement of Cr(III) and Cr(VI) in freshwaters with a single diffusive gradients in thin films device. Talanta 154, 533–538.

Ernstberger, H., Zhang, H., Davison, W., 2002. Determination of chromium speciation in natural systems using DGT. Anal. Bioanal. Chem. 373 (8), 873–879.

Fan, X.F., Ding, S.M., Chen, M.S., Gao, S., Fu, Z., Gong, M.D., Tsang, D.C.W., Wang, Y., Zhang, C.S., 2019. Peak chromium pollution in summer and winter caused by high mobility of chromium in sediment of a eutrophic lake:in situ evidence from high spatiotemporal sampling. Environ. Sci. Technol. 53 (9), 4755–4764.

Fang, W., Shi, X.Y., Yang, D.X., Hu, X., Williams, P.N., Shi, B.Q., Liu, Z.D., Luo, J., 2020. In situ selective measurement based on diffusive gradients in thin films technique with mercapto-functionalized mesoporous silica for high-resolution imaging of SbIII in soil. Anal. Chem. 92 (5), 3581–3588.

Ferreira, N.S., Oliveira, L.H.B., Agrelli, V., de Oliveira, A.F., Nogueira, A.R.A., Oliveira, A., Gonzalez, M.H., 2018. Bioaccumulation and acute toxicity of AsIII and AsV in Nile tilapia (Oreochromis niloticus). Chemosphere 217, 349–354.

Glud, R.N., Ramsing, N.B., Gundersen, J.K., Klimant, I., 1996. Planar optodes: a new tool for fine scale measurements of two-dimensional O2 distribution in benthic communities. Mar. Ecol. Prog. Ser. 140 (1–3), 217–226.

Gorny, J., Billon, G., Noiriel, C., Dumoulin, D., Lesven, L., Madé, B., 2017. Chromium behavior in aquatic environments: a review. Environ. Rev. 24 (4), 503–516.

Herath, I., Vithanage, M., Bundschuh, J., 2017. Antimony as a global dilemma: geochemistry, mobility, fate and transport. Environ. Pollut. 223, 545–559.
Jørgensen, B.B., Nelson, D.C., 2004. Sulfide oxidation in marine sediments: geochemistry meets microbiology [M]. Sulfur Biogeochemistry-Past and Present. Geological Society of America, pp. 63–81.
Kimbrough, D.E., Cohen, Y., Winer, A.M., Creelman, L., 1999. A critical assessment of chromium in the environment. Crit. Rev. Environ. Sci. Technol. 29 (1), 1–46.
Koren, K., Zieger, S.E., 2021. Optode based chemical imaging—possibilities, challenges, and new avenues in multidimensional optical sensing. ACS Sensors 6 (5), 1671–1680.
Larsen, M., Borisov, S.M., Grunwald, B., Klimant, I., Glud, R.N., 2011. A simple and inexpensive high resolution color ratiometric planar optode imaging approach: application to oxygen and pH sensing. Limnol. Oceanogr. Methods 9, 348–360.
Lee, K.S., Shim, H.Y., Lee, D.S., Chung, D.Y., 2015. The fate and factors determining arsenic mobility of arsenic in soil-a review. Korean J. Soil Sci. Fertil. 48 (2), 73–80.
Lehto, N.J., 2012. The use of ultra-thin diffusive gradients in thin-films (DGT) devices for the analysis of trace metal dynamics in soils and sediments: a measurement and modelling approach. Environ. Chem. 9 (4), 415–423.
Leuz, A.K., Mönch, H., Johnson, C.A., 2006. Sorption of SbIII and SbV to goethite: influence on SbIII oxidation and mobilization. Environ. Sci. Technol. 40 (23), 7277–7282.
Li, C., Ding, S.M., Yang, L.Y., Wang, Y., Ren, M.Y., Chen, M.S., Fan, X.F., Lichtfouse, E., 2018. Diffusive gradients in thin films: devices, materials and applications. Environ. Chem. Lett. 17, 801–831.
Li, C., Ding, S.M., Yang, L.Y., Zhu, Q., Zhang, C.S., 2019. Planar optode: a two-dimensional imaging technique for studying spatial-temporal dynamics of solutes in sediment and soil. Earth Sci. Rev. 197, 102916.
Li, B.R., Liao, P., Xie, L., Li, Q.Q., Pan, C., Ning, Z.G., Liu, C.X., 2020. Reduced NOM triggered rapid CrVI reduction and formation of NOM-CrIII colloids in anoxic environments. Water Res. 181, 115923.
Martin, B.C., Bougoure, J., Ryan, M.H., Bennett, W.W., Colmer, T.D., Joyce, N.K., Olsen, Y.S., Kendrick, G.A., 2018. Oxygen loss from seagrass roots coincides with colonisation of sulphide-oxidising cable bacteria and reduces sulphide stress. ISME J. 13 (3), 707–719.
Marzocchi, U., Benelli, S., Larsen, M., Bartoli, M., Glud, R.N., 2019. Spatial heterogeneity and short-term oxygen dynamics in the rhizosphere of Vallisneria spiralis: implications for nutrient cycling. Freshw. Biol. 64 (3), 532–543.
Ren, M.Y., Ding, S.M., Fu, Z., Yang, L.Y., Wang, Y., 2018. Seasonal antimony pollution caused by high mobility of antimony in sediments: in situ evidence and mechanical interpretation. J. Hazard. Mater. 367, 427–436.
Ren, M.Y., Ding, S.M., Dai, Z.H., Wang, J.F., Wang, Y., 2021. A new DGT technique comprising a hybrid sensor for the simultaneous high resolution 2-D imaging of sulfides, metallic cations, oxyanions and dissolved oxygen. J. Hazard. Mater. 403, 123597.
Santner, J., Larsen, M., Kreuzeder, A., Glud, R.N., 2015. Two decades of chemical imaging of solutes in sediments and soils–a review. Anal. Chim. Acta 878, 9–42.
Shi, X.Y., Fang, W., Tang, N., Williams, P.N., Hu, X., Liu, Z.D., Yin, D.X., Ma, L.Q., Luo, J., 2018. In situ selective measurement of SeIV in waters and soils: diffusive gradients in thin-films with bi-functionalized silica nanoparticles. Environ. Sci. Technol. 52 (24), 14140–14148.
Smolders, E., Wagner, S., Prohaska, T., Irrgeher, J., Santner, J., 2020. Sub-millimeter distribution of labile trace element fluxes in the rhizosphere explains differential effects of soil liming on cadmium and zinc uptake in maize. Sci. Total Environ. 738, 140311.
Sun, W.M., Xiao, E.Z., Krumins, V., Häggblom, M.M., Dong, Y., Pu, Z., Li, B., Wang, Q., Xiao, T., 2018. Rhizosphere microbial response to multiple metal(loid)s in different contaminated arable soils indicates crop-specific metal-microbe interactions. Appl. Environ. Microbiol. 84 (24), e00701-18.
Wagner, S., Hoefer, C., Prohaska, T., Santner, J., 2020. Two-dimensional visualization and quantification of labile, inorganic plant nutrients and contaminants in soil. JoVE (J. Vis. Exp.) 163, e61661.
Wagner, S., Hoefer, C., Puschenreiter, M., Wenzel, W.W., Santner, J., 2020. Arsenic redox transformations and cycling in the rhizosphere of Pteris vittata and Pteris quadriaurita. Environ. Exp. Bot. 177, 104122.
Wang, Y., Ding, S.M., Gong, M.D., Xu, S.W., Xu, W.M., Zhang, C.S., 2016. Diffusion characteristics of agarose hydrogel used in diffusive gradients in thin films for measurements of cations and anions. Anal. Chim. Acta 945, 47–56.
Wang, L.Y., Ye, L., Yu, Y.Q., Jing, C.Y., 2018. Antimony redox biotransformation in the subsurface: effect of indigenous SbV respiring microbiota. Environ. Sci. Technol. 52 (3), 1200–1207.
Wang, N., Li, Q., Jiang, M.Q., Zhang, W.Z., Zhang, H., Song, Q.X., Hu, Z.D., Zhang, J.B., Zheng, Z., 2020. Effects of distinct revegetation methods on growth and microbial properties of Vallisneria natans. Water 12 (5), 1294.
Warnken, K.W., Zhang, H., Davison, W., 2004. Analysis of polyacrylamide gels for trace metals using diffusive gradients in thin films and laser ablation inductively coupled plasma mass spectrometry. Anal. Chem. 76 (20), 6077–6084.
Zhang, H., Davison, W., 1995. Performance characteristics of diffusion gradients in thin films for the in situ measurement of trace metals in aqueous solution. Anal. Chem. 67 (19), 3391–3400.
Zhu, Q., 2019. In situ planar optical sensors for sediment diagenesis study. Encyclopedia of Ocean Sciences. 4, pp. 147–156.
Zhu, F., Baker, D., Skommer, J., Sewell, M., Wlodkowic, D., 2015. Real-time 2D visualization of metabolic activities in zebrafish embryos using a microfluidic technology. Cytometry Part A 87 (5), 446–450.